PAPER

Capacitive sensing of droplets for microfluidic devices based on thermocapillary actuation

Jian Z. Chen,[a] Anton A. Darhuber,[b] Sandra M. Troian*[b] and Sigurd Wagner[a]

[a] *Department of Electrical Engineering, Department of Chemical Engineering, Princeton University, Princeton, NJ 08544, USA*

[b] *Microfluidic Research & Engineering Laboratory, Department of Chemical Engineering, Princeton University, Princeton, NJ 08544, USA. E-mail: stroian@princeton.edu*

Received 5th December 2003, Accepted 4th May 2004
First published as an Advance Article on the web 25th June 2004

The design and performance of a miniaturized coplanar capacitive sensor is presented whose electrode arrays can also function as resistive microheaters for thermocapillary actuation of liquid films and droplets. Optimal compromise between large capacitive signal and high spatial resolution is obtained for electrode widths comparable to the liquid film thickness measured, in agreement with supporting numerical simulations which include mutual capacitance effects. An interdigitated, variable width design, allowing for wider central electrodes, increases the capacitive signal for liquid structures with non-uniform height profiles. The capacitive resolution and time response of the current design is approximately 0.03 pF and 10 ms, respectively, which makes possible a number of sensing functions for nanoliter droplets. These include detection of droplet position, size, composition or percentage water uptake for hygroscopic liquids. Its rapid response time allows measurements of the rate of mass loss in evaporating droplets.

I Introduction and background

An important feature of microfluidic devices is the significant reduction in liquid volume necessary for chemical and biomolecular diagnostics. Open format devices, which allow fluidic manipulation on the exterior surface of glass or silicon substrates, provide a particularly flexible approach to liquid handling in the nanoliter volume range. Some of the more popular techniques for propelling and manipulating liquid structures in open microfluidic devices include electrowetting,[1–6] dielectrophoresis[7] and thermocapillary actuation.[8–11] Extending the capabilities of these devices to include, for example, automated control over liquid positioning, size and composition, however, will require the integration of miniaturized sensors with fluidic chips.

Capacitive sensors provide a particularly attractive option since the method of detection is non-intrusive, highly sensitive and suitable for electrically conducting or insulating liquids.[12] These advantages have been exploited for measuring liquid volume,[13] mass loss due to liquid evaporation,[14] microbubble size,[15] liquid fill levels,[16] multilayers of different materials,[17] void fraction in liquid–gas two-phase flows,[18] contact angles and droplet speed in electrowetting based propulsion,[19] and the surface tension and chemical composition of small liquid volumes.[20] The majority of these capacitive detectors require an external impedance analyzer, making it difficult to incorporate directly into a small microfluidic device.

Coplanar electrode arrays can offer a more compact design. The conductance (or likewise capacitance) corresponding to a coplanar electrode pair situated beneath a thin layer of material was investigated by Coney.[21] Further studies have shown that the use of interdigitated electrode arrays can substantially increase the capacitive signal, an important consideration when sensing ultrasmall liquid volumes or dilute concentrations. The performance of interdigitated arrays consisting of metallic electrodes of uniform width has been investigated by a number of groups.[17,22–24] These configurations are most suited to sensing dielectric films of uniform height. Most recently, capacitance measurements have been coupled with electrowetting actuation for volume control in droplet dispensing.[25]

During the past few years, we have developed an open microfluidic device in which electronically addressable, substrate embedded microheaters are used to heat selective regions of a glass surface. When a small liquid structure overlays the heating array, the thermal distribution applied to the substrate is directly transferred by conduction through the thin liquid film to the air–liquid interface. The resulting shear stresses at the free interface drive liquid from warmer to cooler regions of the substrate. This method of actuation has successfully been used to mobilize, split, coalesce, trap and even mix liquid samples.[8–11] The actual trajectories of the liquid streams or droplets is further refined by chemical treatment of the glass substrate to prevent undesirable lateral or streamwise spreading. This combination of thermofluidic actuation and surface chemical patterning allows numerous programmable fluidic functions to be carried out precisely and efficiently.

The focus of this current work is the design and development of capacitance microsensors which can be directly integrated with the current fluidic platform. The design of choice allows the electrode arrays to be used either as resistive microheaters for thermocapillary actuation or as capacitive sensors for liquid detection and analysis. The interdigitated, variable width electrode arrays maximize the capacitive signal when handling liquid structures with non-uniform height like droplets or rivulets. We describe the performance of an RC relaxation oscillator sensing circuit, whose capacitance and resonance frequency register a measurably large shift in response to an overlying liquid film. An analysis of the electric field distribution corresponding to a parallel, coplanar semi-infinite pair of electrodes is used to illustrate the importance of the field penetration depth and effective electrode width in designing sensor layouts suitable for use with small liquid volumes of non-uniform thickness. The results of various experimental tests confirm that the capacitive sensor described below can be calibrated to detect droplet size, location, composition, rate of evaporative mass loss and rate of water absorption for hygroscopic liquids. The proposed design presents a satisfactory compromise between a large signal to noise ratio and high spatial resolution.

DOI: 10.1039/b315815b

II Analytical model for coplanar capacitive sensing

A simplified analysis for computing the capacitance corresponding to a pair of semi-infinite electrodes is first used to introduce two important design variables, namely the field penetration depth and the effective electrode width. As shown in Fig. 1, two parallel, coplanar and semi-infinite conducting films separated by a gap distance $2a$ are embedded within a uniform dielectric medium of permittivity ε_r, each held at a constant potential $\pm V_0$. The two-dimensional electric field distribution for this geometry can be conveniently solved by conformal mapping techniques using an inverse-cosine transform,[26] as outlined in the Appendix. These results for semi-infinite electrodes can be used to compute the capacitance of an electrode pair of finite width, w, according to

$$C = \frac{Q}{2V_0} = \frac{2\varepsilon_r\varepsilon_0 l}{\pi}\ln\left[\left(1+\frac{w}{a}\right)+\sqrt{\left(1+\frac{w}{a}\right)^2-1}\right] \qquad (1)$$

where Q is the total charge on a single electrode, ε_0 is the vacuum permittivity, and l is the length of the electrode pair (in the z direction) for $l \gg w$. Eqn. (1) provides a reliable estimate of the capacitance for a coplanar electrode pair of finite width provided $w/a \gg 1$.

The lateral extent of the sensing electrodes, w, establishes a maximum field penetration depth, T, (in the $\hat{y}$ direction) into the embedding medium whose thickness will be designated by d_{liq}, for liquid-like dielectric films. The penetration depth can be deduced from the elliptical contours, $v(x, y)$, corresponding to the field strength at a position $r = \sqrt{(x^2 + y^2)}$ (see Appendix), as shown in Fig. 1(b). This penetration length, T, corresponds to the maximum vertical displacement ($\hat{y}$ axis) of the field line emanating from the outermost edge of the electrode pair:

$$T = a\sinh\left[\cosh^{-1}\left(1+\frac{w}{a}\right)\right] = a\sqrt{\left(1+\frac{w}{a}\right)^2-1} \qquad (2)$$

For liquid films whose thickness $d_{liq} < T$, the capacitance is only determined by those electric field lines emanating from the effective portion of the electrode widths designated by w_{eff} in Fig. 1(c). Re-expression of eqn. (2) for this case leads to the relation

$$\frac{w_{eff}}{a} = \cosh\left[\sinh^{-1}\left(\frac{d_{liq}}{a}\right)\right]-1 = \sqrt{1+\left(\frac{d_{liq}}{a}\right)^2}-1 \qquad (3)$$

This concept of an effective electrode width is only applicable when the permittivity of the embedding dielectric medium is much greater than that of air, as is true for the liquid films considered in this work. In the extreme limit where $d_{liq} \gg T$ or $d_{liq} \ll T$, however, the capacitive signal will be greatly reduced. In the former case, the liquid film beyond the vertical position $y = T$ is only weakly probed by the electrical field lines; in the latter case, the signal level will be sharply diminished because the dielectric volume probed is very small. The ratio d_{liq}/T therefore serves as a rough indicator of the signal level detectable for this electrode geometry.

An optimal compromise between a large signal to noise ratio and high spatial resolution can be achieved when the lateral extent of the sensing electrodes, w, is comparable to the maximum liquid film height, d_{liq}, expected for a given application. In this case, the maximum capacitance, C_{opt}, corresponding to an embedding medium of thickness, d_{liq}, is given by substitution of eqn. (3) into eqn. (1):

$$C_{opt} = \frac{\varepsilon_r\varepsilon_0 l}{\pi}\ln\left\{\sqrt{1+\left(\frac{d_{liq}}{a}\right)^2}+\frac{d_{liq}}{a}\right\} \qquad (4)$$

This relation suggests that the maximum capacitive signal can be achieved by minimizing the electrode gap spacing, $2a$, while fabricating electrodes whose width is comparable to the thickness of the embedding layer to be measured. In contrast to a parallel plate capacitor, the capacitance C does not increase in proportion to w/a but only in proportion to $\ln(w/a)$ as $w/a \rightarrow \infty$.

The derivation leading to eqn. (1) is strictly valid in the limit $w/a \gg 1$. To determine the validity of this equation for a wider range of ratios $1 \leqslant w/a \leqslant 1000$, we conducted simulations with FemLab 2.2 using the geometry shown in the inset of Fig. 1(d). All materials were assumed to be either perfect conductors or perfect insulators such that Maxwell's equation simplified to the form $\nabla^2 u(x, y) = 0$, where u denotes the electrical potential function. The electrical potentials were set to be $u(a \leqslant x \leqslant a + w, y = 0) = V_0$ and $u(-a \leqslant x \leqslant -(a + w), y = 0) = -V_0$. The normal component of the displacement vector, $\boldsymbol{n}\cdot\boldsymbol{D}$, where $\boldsymbol{n}$ is the unit normal vector pointing outward from the computational domain, was set to vanish on all other boundaries. The total capacitance was computed according to $C = Q_{tot}/2V_0$, where Q_{tot} denotes the total charge on a single electrode and $2V_0$ represents the voltage difference between the electrode pair. The solid line in Fig. 1(d) corresponds to the analytic solution given by eqn. (1); the filled symbols represent the simulation results for three different electrode widths (w = 100, 500 and 1000 μm) and varying values of the electrode gap spacing $2a$. The deviation between the analytic result for semi-infinite electrodes and the numerical results corresponding to

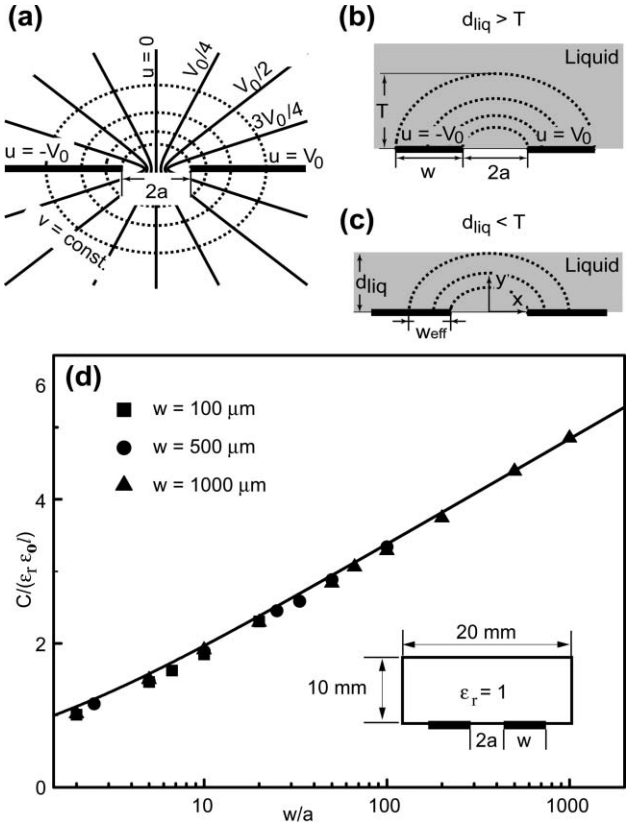

Fig. 1 (a) Contour lines representing solutions of the electrical potential u (solid lines) and electric flux v (dotted lines) for two coplanar, semi-infinite conducting plates separated by a distance $2a$ and held at constant potential $\pm V_0$. (b) Field penetration depth, T, for conducting plates of finite width, w, embedded in a dielectric liquid film of thickness $d_{liq} > T$. (c) Effective electrode width, w_{eff}, for the case where $d_{liq} < T$. The width w_{eff} is defined by the intersection of the electric flux solution passing through ($x = 0$, $y = d_{liq}$) with the plane $x = 0$. (d) Comparison of the capacitance per unit length l obtained from full numerical simulations (solid symbols—geometry shown by inset) with the approximate solution given by eqn. (1) (solid line).

finite width electrodes is everywhere rather small. The most significant deviation occurs for the smallest ratios w/a. For instance, the ratio w/a = 1.1 produces a deviation from the semi-infinite approximation of approximately 10.4%, whose value decreases to about 0.2% for w/a = 1000. These simulations therefore confirm that eqn. (1) can be used as an excellent approximation for the capacitance even for ratios w/a close to unity.

III Sensor circuit layout and experimental setup

A parallel, coplanar electrode pair of length l, width w and gap spacing $2a$ can serve as a capacitance sensor when connected in parallel to an RC-relaxation oscillatory circuit consisting of two invertors (Philips 74HC04), a resistor, R_c, and a capacitor, C_c. For these experiments, C_c and R_c were chosen to be 10 pF and 105.1 kΩ, respectively. The coplanar electrodes were fabricated to be 16 mm long and either 100 or 200 μm wide, with a separation distance $2a$ = 60 or 120 μm. The metal electrodes were deposited by electron beam evaporation of 10 nm Ti followed by 200 nm Au on a 0.5 mm thick Corning 1737F glass substrate. The electrode patterns were defined by photolithography and lift-off; the masks were printed with a high resolution image setter on transparent polymer foils. After deposition, the metal electrodes were passivated by plasma-enhanced chemical vapor deposition of 0.8 μm of SiO_2.[9,10]

As shown in Fig. 2(a), the RC circuit is connected in parallel to a larger support assembly whose overall capacitance is designated by C_{sys}^{α}, where α = liq or air and denotes whether the embedding medium in the half-space above the electrode pair was covered by a liquid film or air. The entire assembly including the embedded electrode pair is shown in Fig. 2(b). A more detailed breakdown of the component layers within the positioning stage is shown in Fig. 2(c). This same layered geometry was used in the numerical computations of the overall capacitance to be described next. The capacitance difference with and without the liquid layer, ΔC_{liq}, was measured with a Keithley 2000 multimeter by monitoring the resonant frequency shift[28] according to

$$\Delta C_{liq} = C_{sys}^{liq} - C_{sys}^{air} = \frac{1}{2\ln(3)}\left(\frac{1}{f} - \frac{1}{f_0}\right)\frac{1}{R_c} \qquad (5)$$

where f and f_0 represent the sensor output frequencies with and without an overlying liquid film. Despite significant shielding, the resonance frequency f_0 = 370 kHz was still observed to fluctuate rapidly by about 0.1 kHz and to drift slowly by about 1 kHz. This drift corresponded to a capacitance resolution of 0.03 pF, which established the smallest value measurable with our device. The frequency dependence of the permittivity of liquid films was negligible in our measurements since the operating frequencies only spanned a maximum range of approximately 100 kHz.

The electronic circuit was calibrated by measuring the capacitance shift with a known film thickness of glycerol positioned within the micrometer stage, as shown in Fig. 2(b). For mechanical stability, the glass substrate containing the metal electrode pair was rigidly held in place by a brass vacuum chuck. The large brass block and micrometer stage established electrical ground. The thickness of the glycerol layer was adjusted by positioning a polycarbonate sheet beneath the underside of the top plate of the micrometer stage. The micrometer reading was tared to zero when the polycarbonate sheet contacted the surface of the glass slide. In this way, the film thickness, d_{liq}, could be controlled to an accuracy of 10 μm.

Three polar liquids were used in the experimental studies, namely glycerol (1,2,3-trihydroxy propane, $C_3H_8O_3$, Aldrich, purity 99%), TEG (tetraethylene glycol, $C_{18}H_{38}O_5$, Aldrich, purity 99%) and distilled, doubly deionized water (Hydro

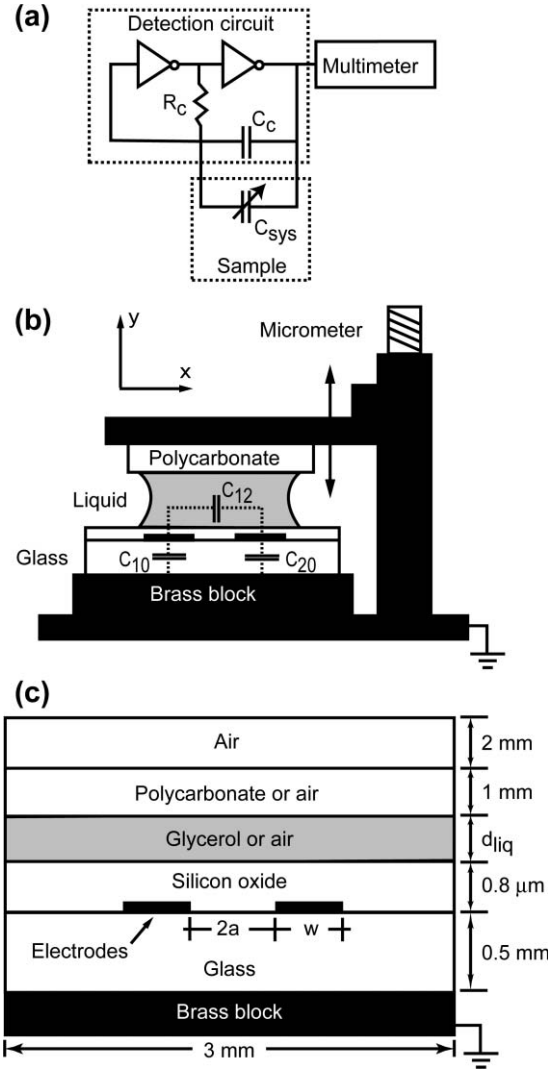

Fig. 2 (a) Schematic diagram of the complete sensing circuit consisting of two inverters, one resistor R_c and one capacitor C_c, which are attached in parallel to the system shown in (b) whose capacitance is given by C_{sys}. Changes in C_{sys} detectable by the oscillation frequency shift are measured with an external multimeter. (b) Schematic diagram of the experimental setup containing the sensing electrode arrays. The liquid film thickness, d_{liq}, is adjusted by vertical displacement of a (non-wetting) polycarbonate sheet. The native electrode pair capacitance is denoted C_{12}; the coupling capacitances with the brass block are labelled C_{10} and C_{20}. (c) Computational domain used for the numerical simulations. The relative permittivities of the materials were chosen to be 45.5 for glycerol (10% water content),[27] 5.7 for Corning 1737F glass[29] and 3.0 for the polycarbonate sheet.[30]

Ultra-Pure water system, 18 MΩ resistivity). Both glycerol and TEG have low vapor pressures at standard temperature and pressure and were therefore considered non-volatile. Glycerol and TEG, however, are hygroscopic liquids whose permittivity increases with water absorption. The refractive index of glycerol was measured with an Abbé refractometer before and after each experiment in order to monitor the level of water uptake. The refractive index varied between approximately 1.4617 and 1.4577, indicating a water content ranging from 8–10 wt%.[27] The dielectric constant was therefore expected to vary between 44.42 and 45.50, a difference that was not detectable by the sensing circuit used. This level of water content is the expected equilibrium value for temperatures ranging from 20–25 °C at a relative humidity of 40–50%. All experimental measurements were completed within a 20 minute interval in order to minimize the influence of

water or carbon dioxide absorption and other contaminant effects.

IV Numerical simulations including mutual capacitance effects

Peripheral components to the sensing electrodes, like the supporting brass block, essentially generate a three-electrode system, for which mutual capacitance effects must be evaluated. In any system containing several conducting objects, electrical field lines originating from one conductor may terminate on the surface of any other conductor. The effective capacitance between any two conductors therefore includes third-conductor capacitive coupling.[26] The mutual capacitance between conductors i and j is defined by $C_{ij} = Q_j/(V_j - V_i)$, where Q_j is the total surface charge on the j-th conductor and V_i and V_j are the (fixed) electrical potentials corresponding to conductors i and j. According to Fig. 2(b), if C_{12} denotes the capacitance between the electrode pair and $C_{10} = C_{20}$ denotes the capacitance between the individual electrodes and the brass block, the effective three electrode capacitance is given by $C_{sys} = C_{12} + C_{10}$.

Numerical simulations were used to determine the total capacitive shift corresponding to the geometric layout shown in Fig. 2(c). The domain size of the computational cell was chosen to be sufficiently large to ensure that the solutions were insensitive to finite size effects. Mutual capacitances were computed by setting the potential of electrode 1 to 1 V and the potentials of electrode 2 and the bottom boundary of the glass sample to 0 V. All other boundaries were maintained at zero charge density according to $\boldsymbol{n}\cdot\boldsymbol{D} = 0$. The surface charge density on the electrodes was obtained by integrating the electrical displacement vector $\boldsymbol{D}$ along the electrode width.

The capacitance shift, ΔC_{liq}, as defined by eqn. (5), was obtained by considering the effective capacitance of the electrode pair (including mutual capacitance effects) for fixed values of the embedding liquid film thickness, d_{liq}, gap spacing, $2a$, and electrode widths, w. The interstitial layers consisted of either polycarbonate and glycerol or polycarbonate and air. These results were directly compared to experimental measurements for an electrode length l = 16 mm. Fig. 3(a) shows a comparison of the numerical results (open symbols) with experimental measurements (solid symbols) as a function of d_{liq}, for the case of glycerol as the embedding medium. For $2a$ = 60 μm and $d_{liq} \leqslant$ 80 μm, the solutions corresponding to w = 100 and w = 200 μm completely overlap. This behavior is expected since only a portion of the electrodes (where $a \leqslant |x| \leqslant a + w_{eff}$) contribute to the effective capacitance. The capacitive shift is therefore essentially insensitive to electrode widths $w > w_{eff}$. The solutions also indicate that when the liquid film thickness exceeds the penetration depth corresponding to a given electrode width w, the capacitive shift levels off and becomes insensitive to further increases in d_{liq}. In general, the comparison between the measured and computed values is excellent. Additionally, these results show that for fixed electrode widths, a decrease in the gap spacing leads to a larger capacitance shift and therefore higher capacitive signal. As indicated by eqn. (1), the capacitance scales logarithmically with the ratio w/a in the limit $w/a \gg 1$.

V Capacitive sensor functions

The understanding gained from the analysis in the previous section was used to develop a number of sensing functions. We tested two layouts for this purpose, namely symmetric electrode pairs of equal width and an improved design consisting of interdigitated electrodes of variable width. The resistive heating profile and actuation sequence corresponding to the first, simpler design has been described elsewhere.[10] The variable width design allows for higher spatial resolution when sensing liquid structures of non-uniform thickness, such as when detecting liquid streams or droplets with significant interfacial curvature. In what follows, we discuss measurements made using these two types of sensor layouts which, in addition to determination of the film thickness as shown in Fig. 3(a), can also be used to differentiate between different liquids, to measure the level of water absorption in hygroscopic liquids, to determine and monitor droplet location and to evaluate the degree of evaporative mass loss in volatile samples.

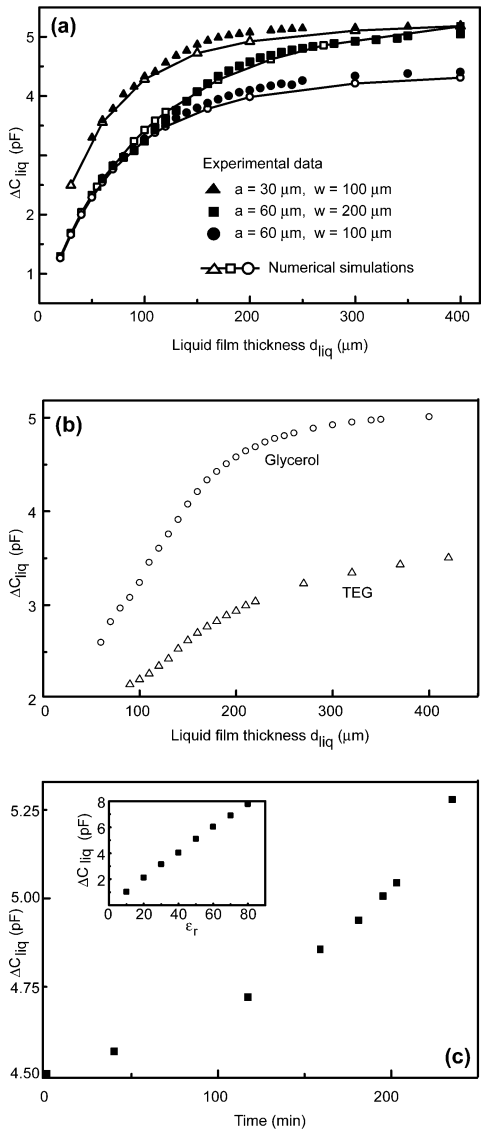

Fig. 3 (a) Comparison of experimental data (solid symbols) and results of numerical simulations (open symbols and solid lines) for glycerol as the (uniform) embedding liquid. The length of the electrodes was 16 mm. The wider electrodes (w = 200 μm, solid squares) generate a larger capacitive signal for the thicker films. (b) Experimental results for glycerol (circles) and TEG (triangles) with $2a$ = 120 μm and w = 200 μm. (c) Capacitance measurement for 250 μm thick film of glycerol for $2a$=120 μm and w = 200 μm as a function of time. The signal increase is caused by water absorption since glycerol is a hygroscopic liquid. Inset: results of numerical simulations, with $2a$ = 120 μm and w = 200 μm and d_{liq} = 250 μm, as a function of the permittivity of the embedding medium, ε_r. The linear dependence of ΔC_{liq} with ε_r allows determination of the composition ratio for completely soluble liquids.

A Liquid sensor for single and binary component mixtures

For a single component liquid film of uniform height and constant permittivity ε_r, the effective capacitance shift ΔC_{liq}, as defined by eqn. (5), is linearly proportional to ε_r. The inset of Fig. 3(c) demonstrates this linearity for a 250 μm thick film of glycerol. This calibration curve can therefore be used to determine the dielectric constant of other types of liquid films. Fig. 3(b) shows measurements of the capacitive shift corresponding to different film thicknesses of glygerol and TEG for a simple, coplanar, two electrode system with $2a = 120$ μm and $w = 200$ μm. The relative permittivity of TEG, obtained from the relation $\varepsilon_{TEG} = \varepsilon_{glycerol} \times \Delta C_{TEG}/\Delta C_{glycerol}$ by averaging the results for all film thicknesses measured, was determined to be $\varepsilon_{TEG}^{meas} = 29.85 \pm 0.95$. As expected, this value is higher than the permittivity of pure TEG reported in the literature,[31] namely $\varepsilon_{TEG}^{o} = 20.44$ at 20 °C due to its hygroscopic nature. For completely soluble mixtures, like glycerol and water or TEG and water, the mixture permittivity is proportional to the weight ratio of the two components.[27,31,32] The percentage of water absorption by TEG can therefore be estimated from the ratio $(\varepsilon_{TEG}^{meas} - \varepsilon_{TEG}^{o})/(\varepsilon_{water} - \varepsilon_{TEG}^{o}) = 15.7$ wt%, where $\varepsilon_{water} = 80.22$ and the superscript "o" represents no water content.[31] The values measured by the sensor are therefore consistent with the expected water uptake for a relative humidity of 40–50%.[32] This level of water content for TEG, however, was slightly higher than the value measured by Abbé refractometry for which the refractive index was 1.4425, indicating 12wt% adsorption content. Fig. 3(c) represents capacitance measurements of a 250 μm thick glycerol film as a function of time. Liquid mixtures for which the permittivity of the individual components leads to a non-linear relation for the total permittivity could also be measured using this technique provided that the non-linear relation is known.

B Droplet position sensor

The introduction of feedback control into microfluidic devices will eventually require determination of simple variables like droplet position, which can ideally be determined by capacitive sensing. In this part of the study, we used a simple linearly distributed array of capacitive electrodes of uniform width which already served as the microheater array for thermocapillary droplet propulsion. The dark vertical stripes shown in Fig. 4(a) represent the individual microheaters/electrodes, which were passivated by an 800 nm layer of silicon oxide (see Fig. 2(c)). The regions shown in grey represent the bare silicon oxide surface which is wettable by the liquids tested. All other regions of the chip surface were chemically treated to repel the liquids tested.[8,10] As shown in Fig. 4(b), the presence of three distinct glycerol droplets of slightly different volume locally increased the capacitive signal along the linear array of electrodes ($w = 800$ μm). The black regions designate the gaps between the microheater/capacitive electrodes. The larger spacings (black notches) near the top and bottom of the image were used to generate a slightly warmer surface temperature for even better lateral confinement during droplet propulsion.[10] In this example, the droplets spanned an extent covering 2–4 electrodes. By decreasing the liquid volume so that each droplet spans at most two electrodes, one can develop a droplet counter by simply measuring the number of capacitive peaks generated along the rectilinear array.

An improved design relying on interdigitated electrodes of variable width was investigated next to increase the capacitive signal obtained. As mentioned in the Introduction, the flow direction for thermocapillary actuation of liquid streams or droplets can be further refined by chemically treating the surface to repel any undesirable spreading. The diagram in Fig. 5(a) represents, for instance, the streaming actuation of a

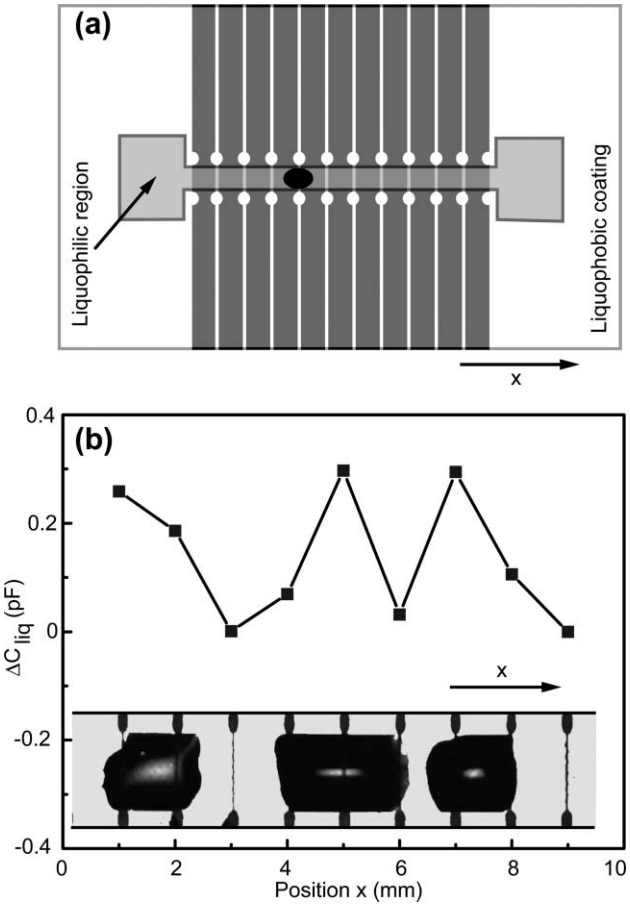

Fig. 4 (a) Schematic diagram of a prototype thermofluidic device in which an embedded electrode array can be used to mobilize or capacitively sense the location, size or composition of an overlying liquid film or droplet. (b) Capacitive signal corresponding to three glycerol droplets of slightly different volume confined by chemical treatment to a 1 mm wide lane. The uniform electrode widths were fabricated to be $w = 800$ μm. The droplets span distances ranging from 2–4 electrodes. The narrow, vertical black stripes represent the spacing between the electrodes.

liquid rivulet from a diamond shaped reservoir along a straight and narrow pathway. The laterally confined liquid in this case assumes a cross-sectional shape $h = h_0(x)(1 - 4z^2/w_c^2)$, where $h_0(x)$ is the liquid apex height (along $z = 0$) and w_c is the microstripe width.[9]

The improved design suitable for sensing liquid elements with non-uniform surface shape is shown in Fig. 5(b) and consists of an interdigitated design with variable width electrodes. The wider electrodes near the center increase the capacitive signal in the region where the liquid film achieves its maximum thickness. The electrode widths at the periphery are narrower by comparison. The smaller widths correspond to electrodes of smaller effective width w_{eff}. In the experiments, the electrode widths from the edges to the center were fabricated to be 60, 80, 135 and 150 μm with a fixed electrode separation of 60 μm. This variable width design resulted in an increased capacitive signal compared to constant width designs without diminishing the spatial resolution required for detecting droplet position. Fig. 5(c) shows the capacitive shift response for three glycerol droplets positioned along a horizontal microstripe of 1 mm width using an embedded electrode array as described in Fig. 5(b). Overall, the signal amplitude increased by almost a factor of two compared to the results shown in Fig. 4. In addition, this design allowed a reduction in electrode spacing to 350 μm, which therefore also increased the spatial resolution to 350 μm. According to

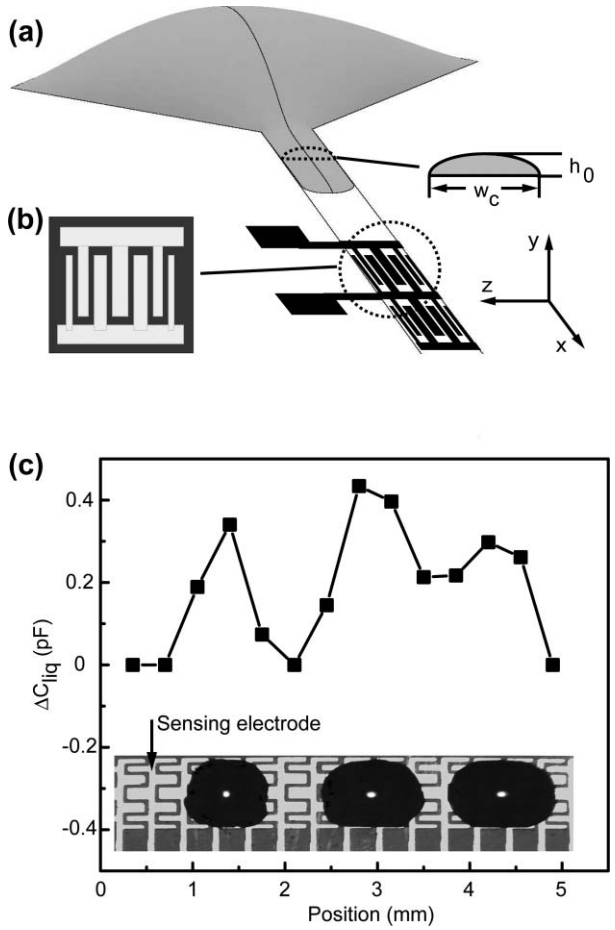

Fig. 5 (a) A representative sketch demonstrating the thermocapillary mobilization of a liquid stream confined to flow along a pathway of width, w_c. The liquid is extracted from the larger (diamond-shaped) reservoir shown in grey. The liquid rivulet assumes a parabolic shape in cross-section with apex height h_0 and width w_c. (b) Magnified view of interdigitated electrodes of variable width. (c) Capacitive signal corresponding to three glycerol droplets of slightly different volume confined by chemical treatment to a 1 mm wide lane. The non-uniform electrode widths from the edge to the center of the sensor were fabricated to be 60, 80, 135 and 150 μm with a fixed electrode spacing of 60 μm. The light grey regions designate the electrode sensing elements; the black gaps designate the spacing in between the interdigitated electrodes.

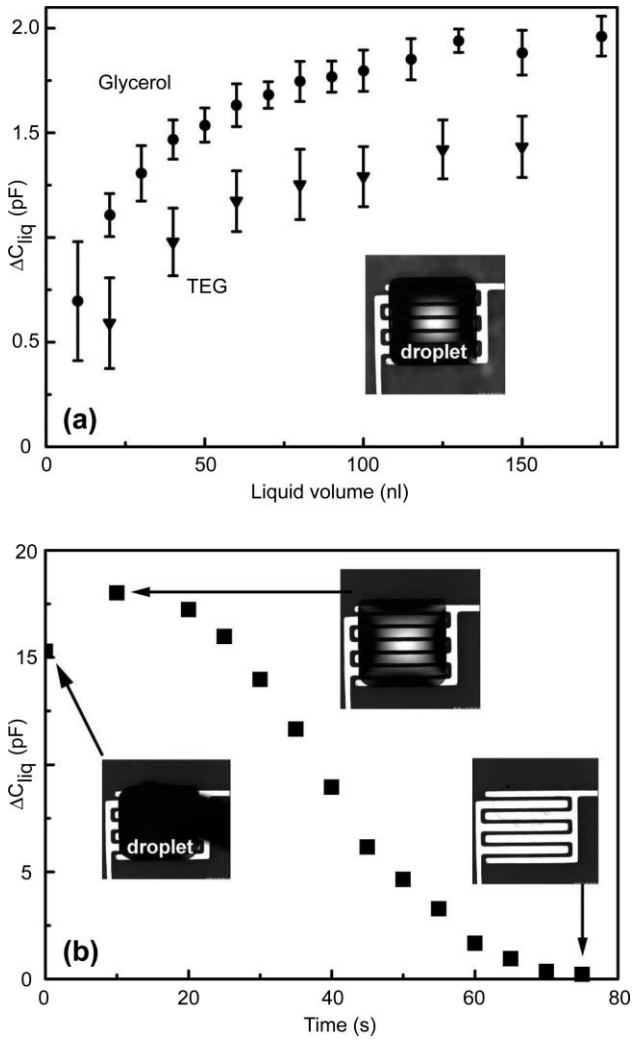

Fig. 6 (a) Capacitive measurement of liquid volume for glycerol (circles) and TEG droplets (triangles) confined to a 1 × 1 mm hydrophilic square. A photograph of the confined liquid residing above an interdigitated sensor is shown in the inset. (b) Decrease of capacitive signal caused by evaporation of a 100 nl water droplet. The photographs were obtained at the time designated by the arrows.

eqn. (4), this spatial resolution can be further improved by reducing the electrode gap spacing, 2*a*.

C Liquid volume sensor

If a droplet can be migrated onto a region of the chip which has been chemically patterned to establish a fixed liquid contact area, then capacitive measurements can be used to determine the liquid volume provided the droplet shape is known. The lower section of Fig. 6(a) shows an optical micrograph of a glycerol droplet of known volume which was deposited onto a square hydrophilic patch (1 mm^2) patterned above a pair of variable width interdigitated electrodes. The measurements shown indicate a clear increase in capacitive signal with increasing liquid volume for droplets of glycerol and TEG. In these experiments, the droplet volume was determined from the digital syringe reading. As expected, this curve is very similar to the experimental measurements and numerical simulations shown previously in Fig. 3(a) for increasing film thickness. The smallest volume probed by this sensing array was approximately 10 nl. This was not the limiting volume detectable by the sensor but only the smallest volume which could be accurately resolved by the digital syringe (Hamilton 7000 series, maximum volume 1 μl) used to deposit the liquid samples. The error bars shown in Fig. 6(a) represent the variation in capacitance measured for seven independent experiments. Most of the error likely stems from the difficulty in dispensing the same exact volume from run to run despite the use of a high quality digital syringe. According to eqn. (4), the minimum detectable volume with a coplanar, equal width electrode pair can be increased by decreasing the electrode gap spacing until quantum effects become important. For the current design shown in Fig. 6(a), the minimum detectable volume was estimated to be 5 nl for complete liquid coverage of the hydrophilic square by a polar liquid like glycerol. This estimate was obtained from numerical simulations in which the volume of a droplet of glycerol at fixed contact area with the solid (1 mm^2) was increased until the total capacitance equalled the minimum detectable value for this sensing circuit (0.03 pF). The maximum detectable volume was approximately 150 nl due to the limitations set by the field penetration depth corresponding to the electrode widths used.

The rapid response time of this capacitive sensor (below 10 ms) suggested it might be possible to measure mass loss in an evaporating droplet. The results shown in Fig. 6(b) for a 100 nl droplet of water at standard temperature and pressure show an initial rise in the capacitive signal at early times followed by a gradual decay. The rise corresponded to the initial coverage

of the hydrophilic square patch by capillary spreading as more of the sensor area became coated with the water film. Eventually the liquid film covered the entire square patch and started to undergo evaporation. Capacitive sensing can therefore be used in applications requiring an evaporation rate monitor and could, for example, be used to determine replenishment levels in chemically reacting systems dependent on fixed mass ratios. Although the relative ambient humidity influences the evaporation rate, it does not directly affect the process by which the capacitance measurement is made. Even at 100% relative humidity at 25 °C, ambient air contains a mere 10^{-3} wt% water, which was not detectable by the sensor electrodes.

VI Summary

For improved and automated performance of numerous liquid handling functions, microfluidic devices will eventually require the use of integrated sensors for detecting such variables as droplet position, volume, composition or mass loss for volumes in the nanoliter range. For compact integration of these sensors into the fluidic platform being developed in our laboratory, it is also desirable to introduce capacitive sensing arrays whose electrodes can also be activated to provide the microresistive heating for thermocapillary actuation when necessary.

A symmetric coplanar electrode design was first investigated to determine what variables affect measurement of the capacitance of an embedding liquid film. Comparison of numerical solutions to experimental measurements confirm the validity of an approximate expression for the capacitance over a wide range of w/a, where w represents the electrode width and $2a$ represents the electrode separation distance. This analysis was also used to illustrate the usefulness of two design variables, namely the field penetration depth and the effective electrode width. The optimal compromise between a large signal to noise ratio and high spatial resolution is obtained in the limit where the electrode widths are made comparable to the thickness of the liquid films to be measured. Further analysis and computations were used to determine the effect of mutual capacitive coupling; these results also compare favorably with experimental measurements. An alternative design, based on interdigitated, variable width electrodes, significantly enhances the capacitance signal and spatial resolution for liquid samples of non-uniform height, as occurs with droplets or rivulets. These studies indicate that capacitive microsensors will prove ever more popular for integration with microfluidic devices based on free surface flow.

Appendix: Approximate solution from consideration of semi-infinite coplanar electrode pair

The two-dimensional electric field distribution corresponding to a single pair of semi-infinite, coplanar conducting plates of infinite length embedded in a dielectric medium of permittivity ε_r (where ε_0 denotes the vacuum permittivity) can be conveniently solved by conformal mapping techniques using the inverse-cosine transform[26]

$$W = V_0 - \frac{2V_0}{\pi}\cos^{-1}\left(\frac{Z}{a}\right) \tag{A1}$$

Here, $W = u(x, y)+\mathrm{i}v(x, y)$, where u is the electrical potential function and v is proportional to the electrical flux function, $2V_0$ represents the fixed potential difference between the two plates and $2a$ represents the electrode gap separation, as shown in Fig. 1. The coordinate position in the complex plane is designated by $Z = x + \mathrm{i}y$. The coordinate values can be rewritten in terms of u and v according to

$$x = a\cos\left[\frac{\pi}{2V_0}(V_0-u)\right]\cosh\left(\frac{\pi}{2V_0}v\right) \tag{A2}$$

$$y = a\sin\left[\frac{\pi}{2V_0}(V_0-u)\right]\sinh\left(\frac{\pi}{2V_0}v\right) \tag{A3}$$

Eqn. (A2) and (A3) can be combined into elliptic or hyperbolic form, useful for separately inspecting the solutions to u and v:

$$\frac{x^2}{\cosh^2\left(\frac{\pi}{2V_0}v\right)} + \frac{y^2}{\sinh^2\left(\frac{\pi}{2V_0}v\right)} = a^2 \tag{A4}$$

$$\frac{x^2}{\cos^2\left(\frac{\pi}{2V_0}(V_0-u)\right)} - \frac{y^2}{\sin^2\left(\frac{\pi}{2V_0}(V_0-u)\right)} = a^2 \tag{A5}$$

Fig. 1(a) depicts the corresponding contour plots for $u(x, y)$ (solid lines) and $v(x, y)$ (dotted lines).

Differentiation of eqn. (A3) with respect to y gives

$$\frac{1}{a} = \frac{\pi}{2V_0}\frac{\partial u}{\partial y}\cos\left[\frac{\pi}{2V_0}(V_0-u)\right]\sinh\left(\frac{\pi}{2V_0}v\right) + \frac{\pi}{2V_0}\frac{\partial v}{\partial y}\sin\left[\frac{\pi}{2V_0}(V_0-u)\right]\cosh\left(\frac{\pi}{2V_0}v\right) \tag{A6}$$

Along the surface of the electrode defined by ($a \leqslant x \leqslant a + w$, $y = 0$), the electrical potential equals $u = +V_0$ and the normal derivative of the electrical flux must vanish *i.e.* $(\partial v/\partial y)_{y=0} = 0$. Substitution of these limits reduces eqn. (A6) to the form

$$\left(\frac{\partial u}{\partial y}\right)_{y=0} = -\frac{2V_0}{a\pi}\frac{1}{\sinh\left(\frac{\pi}{2V_0}v\right)_{y=0}} \tag{A7}$$

For a coplanar electrode pair of *finite* width w, the total surface charge, Q, on a single electrode can be approximated by integrating the electric displacement vector along the plane $y = 0$, where $\boldsymbol{D}(y = 0) = (-\varepsilon_r\varepsilon_0\,(\partial u/\partial y)_{y=0}, 0)$. Assuming all the electrical charges are localized to the plane $y = 0$,

$$Q = \iint \boldsymbol{D}\cdot\mathrm{d}\boldsymbol{A} = 2l\int_a^{a+w}|\boldsymbol{D}(y=0)|\mathrm{d}x = \frac{4\varepsilon_r\varepsilon_0 V_0}{a\pi}l\int_a^{a+w}\frac{\mathrm{d}x}{\sinh\left(\frac{\pi}{2V_0}v\right)_{y=0}} \tag{A8}$$

where l, the electrode length in the z direction, must satisfy the inequality $l \gg w$. Evaluation of eqn. (A2) at $y = 0$ (where $u = +V_0$) yields the solution $x = a\cosh(\pi v/2V_0)_{y=0}$ which simplifies the integral in eqn. (A8) to give

$$Q = \frac{4\varepsilon_r\varepsilon_0 V_0}{a\pi}l\int_a^{a+w}\frac{1}{\sqrt{\left(\frac{x}{a}\right)^2-1}}\mathrm{d}x = \frac{4\varepsilon_r\varepsilon_0 V_0}{\pi}l\ln\left[\left(1+\frac{w}{a}\right)+\sqrt{\left(1+\frac{w}{a}\right)^2-1}\right] \tag{A9}$$

The total capacitance is then simply determined from the ratio $C = Q/2V_0$, which leads to the final expression in eqn. (1).

The maximum field penetration depth, T, can also be determined from examining the solution to eqn. (A4) in the $x = 0$ plane, which yields the relation $T = a\sinh(\pi v/2V_0)$. Eqn. (A4) can also be evaluated at the rightmost edge of the electrode where $x = a + w$ and $u = +V_0$ to give $a + w = a\cosh(\pi v/2V_0)$. Combining these two results produces

the expression for the field penetration depth given by eqn. (2).

Acknowledgments

The authors gratefully acknowledge financial support for this work from the National Science Foundation (CTS and DMR divisions), US Army TACOM-ARDEC and NASA's Microgravity Fluid Physics Program.

References

1 W. J. J. Welters and L. G. J. Fokkink, *Langmuir*, 1998, **14**, 1535.
2 M. G. Pollack, R. B. Fair and A. D. Shenderov, *Appl. Phys. Lett.*, 2000, **77**, 1725.
3 T. Krupenkin, S. Yang and P. Mach, *Appl. Phys. Lett.*, 2003, **82**, 316.
4 M. G. Pollack, A. D. Shenderov and R. B. Fair, *Lab Chip*, 2002, **3**, 96.
5 J. Lee, H. Moon, J. Fowler, T. Schoellhammer and C.-J. Kim, *Sens. Actuators, A*, 2002, **95**, 259.
6 S. K. Cho, H. Moon and C.-J. Kim, *J. Microelectromech. Syst.*, 2003, **12**, 70.
7 T. Jones, M. Gunji, M. Washizu and M. J. Feldman, *J. Appl. Phys.*, 2001, **89**, 1441.
8 A. A. Darhuber, J. P. Valentino, J. M. Davis, S. M. Troian and S. Wagner, *Appl. Phys. Lett.*, 2003, **82**, 657.
9 A. A. Darhuber, J. M. Davis, S. M. Troian and W. W. Reisner, *Phys. Fluids*, 2003, **15**, 1295.
10 A. A. Darhuber, J. P. Valentino, S. M. Troian and S. Wagner, *J. Microelectromech. Syst.*, 2003, **12**, 873.
11 A. A. Darhuber, J. Z. Chen, J. M. Davis and S. M. Troian, *Philos. Trans. R. Soc. London, Ser. A*, 2004, **362**(1818), 1037.
12 *Semiconductor Sensors*, ed. S. M. Sze, J. Wiley & Sons, New York, 1994.
13 K. T. Hjelt, R. van den Doel, W. Lubking and M. J. Vellekoop, *Sens. Actuators, A*, 2000, **83**, 61.
14 K. T. Hjelt, R. van den Doel, W. Lubking and M. J. Vellekoop, *Sens. Actuators, A*, 2000, **85**, 384.
15 T. Merkel, L. Pagel and H.-W. Glock, *Sens. Actuators, A*, 2000, **80**, 1.
16 F. N. Toth and G. C. M. Meijer, *IEEE Trans. Instrum. Meas.*, 1997, **46**, 2.
17 A. V. Mamishev, S. R. Cantrell, Y. Du, B. C. Lesieutre and M. Zahn, *IEEE Trans. Instrum. Meas.*, 2002, **51**, 1192.
18 K. J. Elkow and K. S. Rezkallah, *Meas. Sci. Technol.*, 1996, **7**, 1153.
19 H. J. J. Verheijen and M. W. J. Prins, *Rev. Sci. Instrum.*, 70, **1999**, 3673.
20 C. H. Wang, A. T. Augousti, J. Mason and N. D. McMillan, *Meas. Sci. Technol.*, 1999, **10**, 19.
21 M. W. E. Coney, *J. Phys. E: Sci. Instrum.*, 1973, **6**, 903.
22 B. C. Lesieutre, A. V. Mamishev, Y. Du, E. Keskiner, M. Zahn and G. C. Verghese, *IEEE Trans. Dielectr. Electr. Insul.*, 2003, **8**, 577.
23 B. Timmer, W. Sparreboom, W. Olthuis, P. Bergveld and A. van den Berg, *Lab Chip*, 2002, **2**, 121.
24 W. Olthuis, W. Streekstra and P. Bergveld, *Sens. Actuators, A*, 1995, **24–25**, 252.
25 H. Ren, R. B. Fair and M. G. Pollack, *Sens. Actuators, B*, 2004, **98**, 319.
26 S. Ramo, J. R. Whinnery and T. Van Duzer, *Fields and Waves in Communication Electronics*, J. Wiley & Sons, New York, 1994.
27 A. A. Newman, *Glycerol*, CRC Press, Cleveland, 1968.
28 A. B. Grebene, *Bipolar and MOS Analog Integrated Circuit Design*, J. Wiley & Sons, New York, 1984.
29 *1737F Material Information*, Corning Advanced Display Products.
30 *Dielectric Constant Guide*, ASI Instrument, Inc.
31 *Handbook of Chemistry and Physics*, CRC Press, New York, 84th edn., 2004.
32 *Tetraethylene Glycol Product Guide*, Union Carbide Corp., Danbury, 2000.